Supporting information

Kinetic square scheme in oxygen-redox battery electrodes

Kosuke Kawai,[1,†] Xiang-Mei Shi,[1] Norio Takenaka,[1,2] Jeonguk Jang,[1] Benoit Mortemard de Boisse,[1] Akihisa Tsuchimoto,[1] Daisuke Asakura,[3] Jun Kikkawa,[4] Masanobu Nakayama,[2,5] Masashi Okubo,[1,2,†] Atsuo Yamada[1,2,*]

[1]Department of Chemical System Engineering, School of Engineering, The University of Tokyo, Hongo 7-3-1, Bunkyo-ku, Tokyo 113-8656, Japan

[2]Elemental Strategy Initiative for Catalysts and Batteries (ESICB), Kyoto University, Nishikyo-ku, Kyoto 615-8245, Japan

[3]National Institute of Advanced Industrial Science and Technology, Tsukuba, Ibaraki 305-8568, Japan

[4]National Institute of Materials Science (NIMS), Tsukuba, Ibaraki 305-0047, Japan

[5]Frontier Research Institute for Materials Science (FRIMS), Nagoya Institute of Technology, Showa-ku, Nagoya, Aichi 466-8555, Japan

*yamada@chemsys.t.u-tokyo.ac.jp

[†]Present address

Department of Electrical Engineering and Bioscience, School of Advanced Science and Engineering, Waseda University, Okubo 3-4-1, Shinjuku-ku, Tokyo 169-0555, Japan

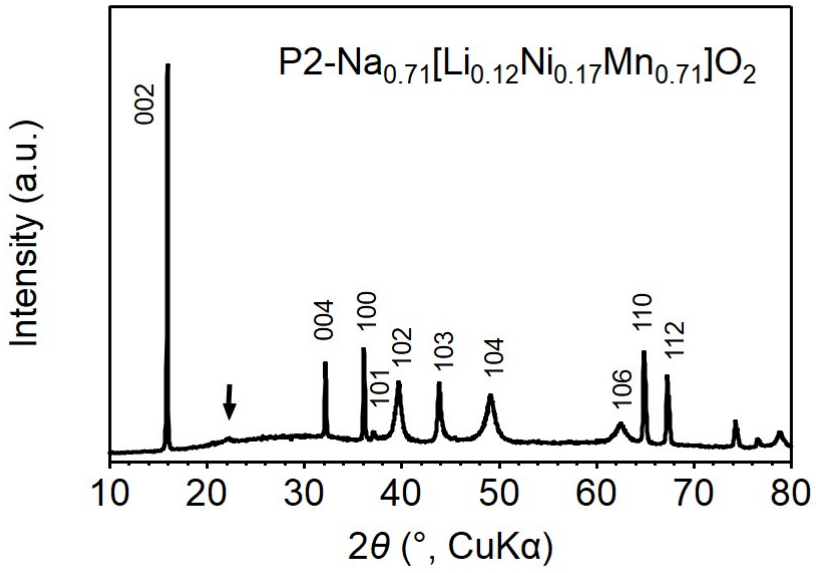

Figure S1. The powder X-ray diffraction pattern of as-prepared P2-$Na_{0.71}[Li_{0.12}Ni_{0.17}Mn_{0.71}]O_2$. Most peaks can be indexed to a hexagonal system (space group: $P6_3/mmc$). A black arrow highlights a superstructure peak arising from in-plane cation ordering.

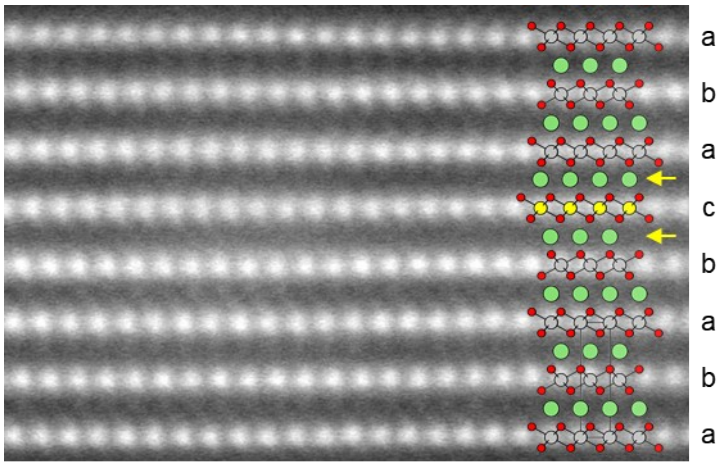

Figure S2. The high-angle annular dark field scanning transmission electron microscopy image of as-prepared O2-$Li_{1.12-y}Ni_{0.17}Mn_{0.71}O_2$. Yellow arrows indicate positions of stacking faults, causing a transition-metal layer 'c' with 'AC'-type oxide-ion packing.

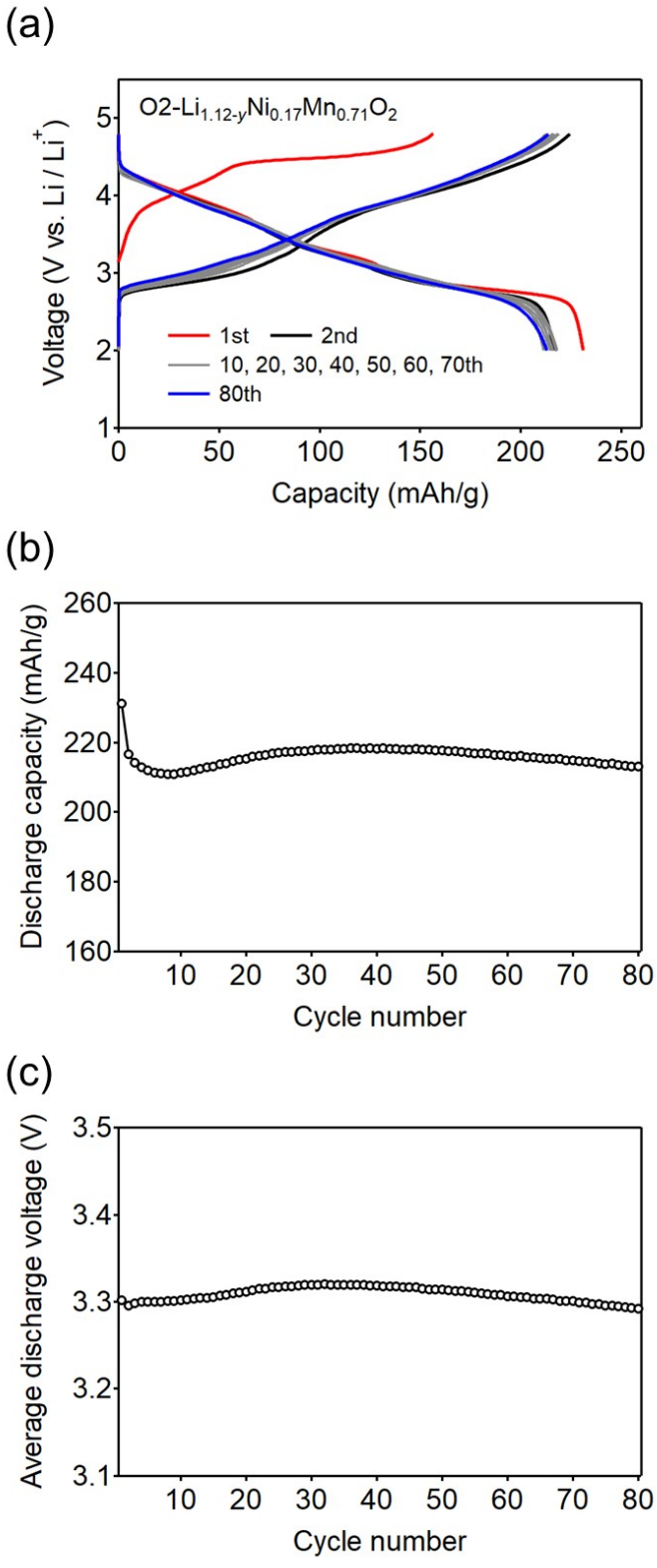

Figure S3. (a) Galvanostatic charge/discharge curves, (b) cycle stability, and (c) average discharge voltage for O2-$Li_{1.12-y}Ni_{0.17}Mn_{0.71}O_2$. Charge/discharge rates are C/20 and C/10 for the first and subsequent cycles, respectively. 1C is defined as 338.2 mA/g.

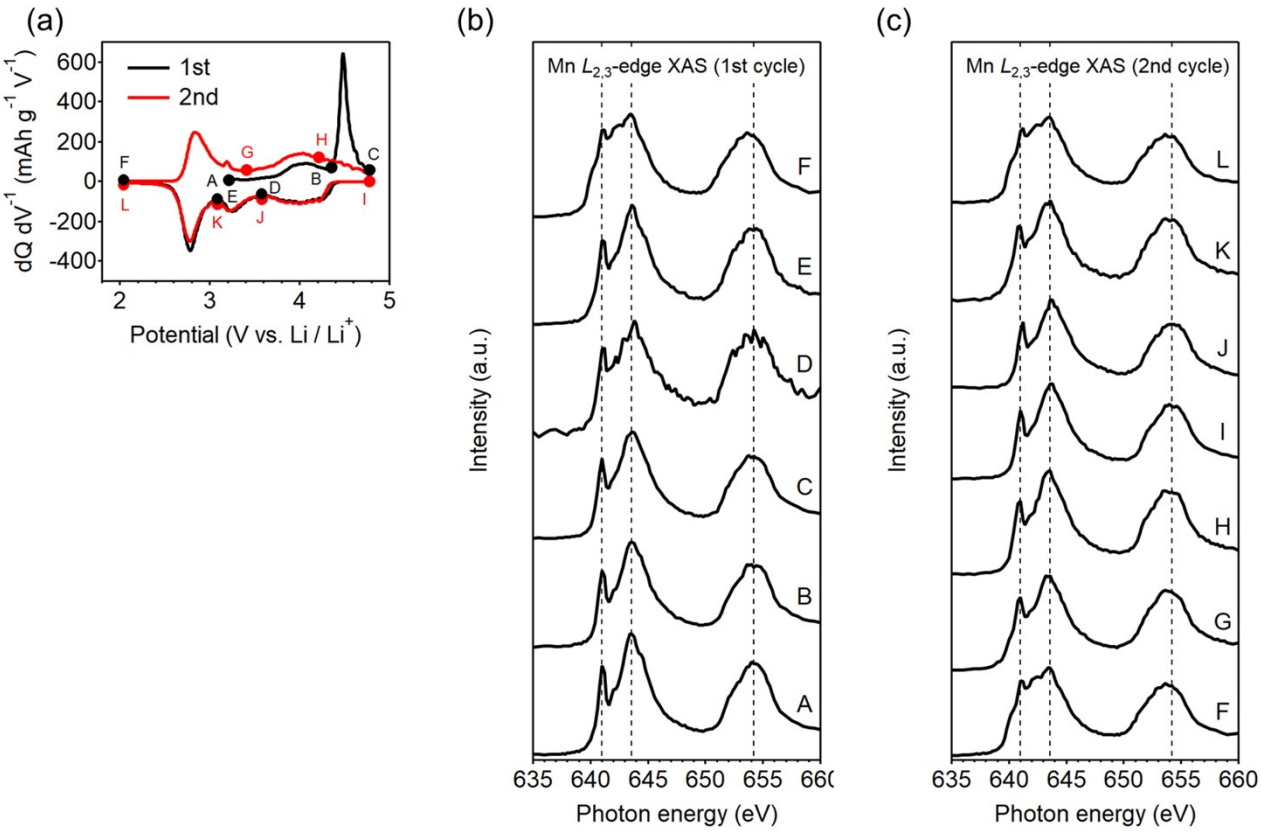

Figure S4. (a) The dQ/dV plots of O2-$Li_{1.12-y}Ni_{0.17}Mn_{0.71}O_2$ during the first and second cycle at the charge/discharge rate of C/20, and *ex situ* Mn $L_{2,3}$-edge X-ray absorption spectra (XAS) during (b) the first and (c) second charge/discharge cycles. For the samples A–E, Mn $L_{2,3}$-edge XAS showed three large peaks at 641.0, 643.6, and 654.2 eV typical for Mn^{4+}. After full discharging (E → F), two new peaks emerged at 640.2 and 642.2 eV, indicating the reduction of Mn^{4+} to Mn^{3+}. The oxidation state of Mn at the end of discharge is approximately estimated as +3.5 according to the literature (Zhou, Z. *et al.*, *Appl. Phys. Lett.* **110**, 093902 (2017)). During the second cycle, Mn^{4+}/Mn^{3+} redox reaction occurs at 2.8 V vs. Li/Li^+ (oxidation: F → G, reduction: K → L). These results are consistent with Mn *K*-edge XANES as shown in Figure 2a and 2d.

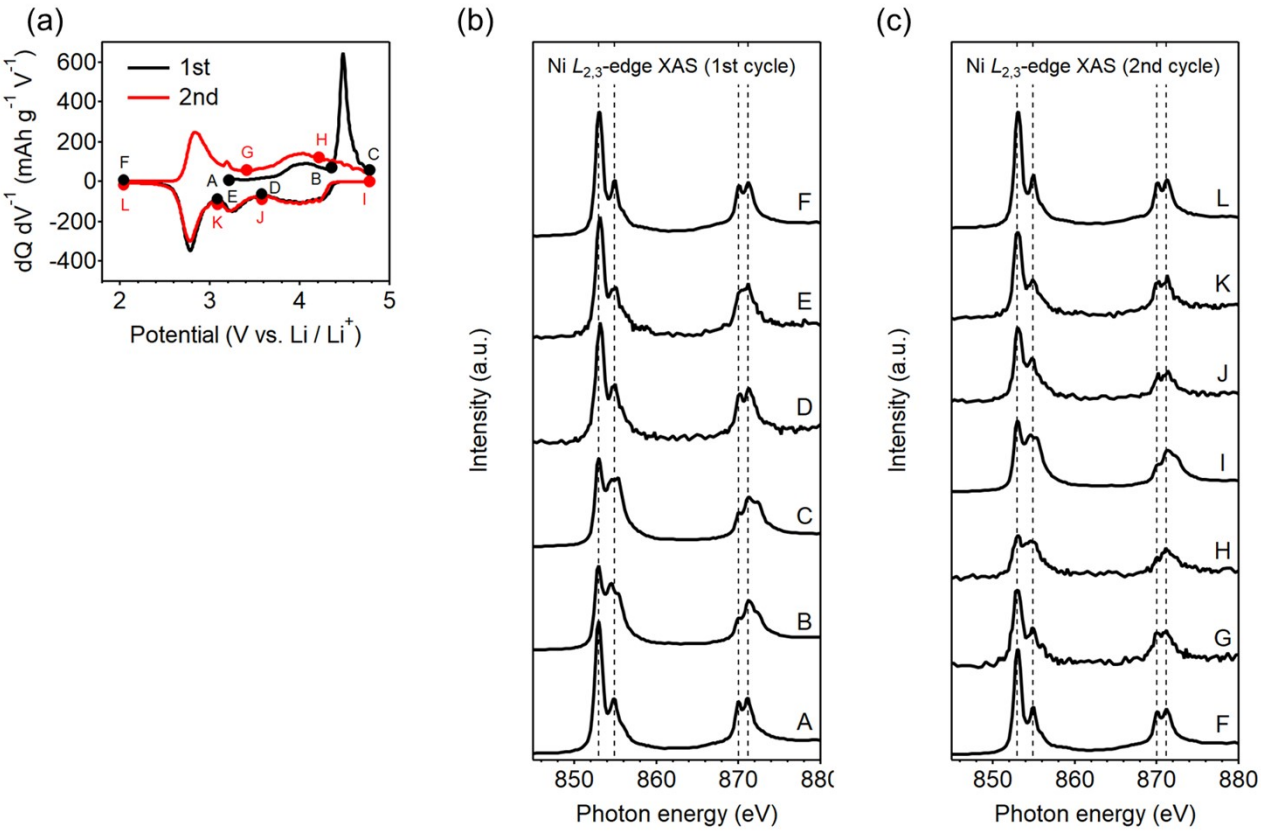

Figure S5. (a) The dQ/dV plots of O2-$Li_{1.12-y}Ni_{0.17}Mn_{0.71}O_2$ during the first and second cycle at the charge/discharge rate of C/20, and *ex situ* Ni $L_{2,3}$-edge X-ray absorption spectra (XAS) during (b) the first and (c) second charge/discharge cycles. At the pristine state, Ni $L_{2,3}$-edge XAS shows four peaks at 853.0, 854.9, 870.1, and 871.2 eV typical for Ni^{2+}. During 1st charging (A → C), intensity of these peaks become weak and two new peaks at 855.5 and 872.5 eV, which are typical for Ni^{3+}, emerge gradually. Note that, in general, Ni^{4+} is unstable even in an inert atmosphere and difficult to be detected in *ex situ* measurements. Upon first discharging, the peaks for Ni^{3+} diminish at 3.6 V vs. Li/Li^+ (D → E). During the second cycle, Ni^{3+}/Ni^{2+} redox reaction occurs at 3.9 V vs. Li/Li^+ (oxidation: G → H, reduction: I → J). These results are consistent with Ni *K*-edge XANES as shown in Figure 2b and 2c.

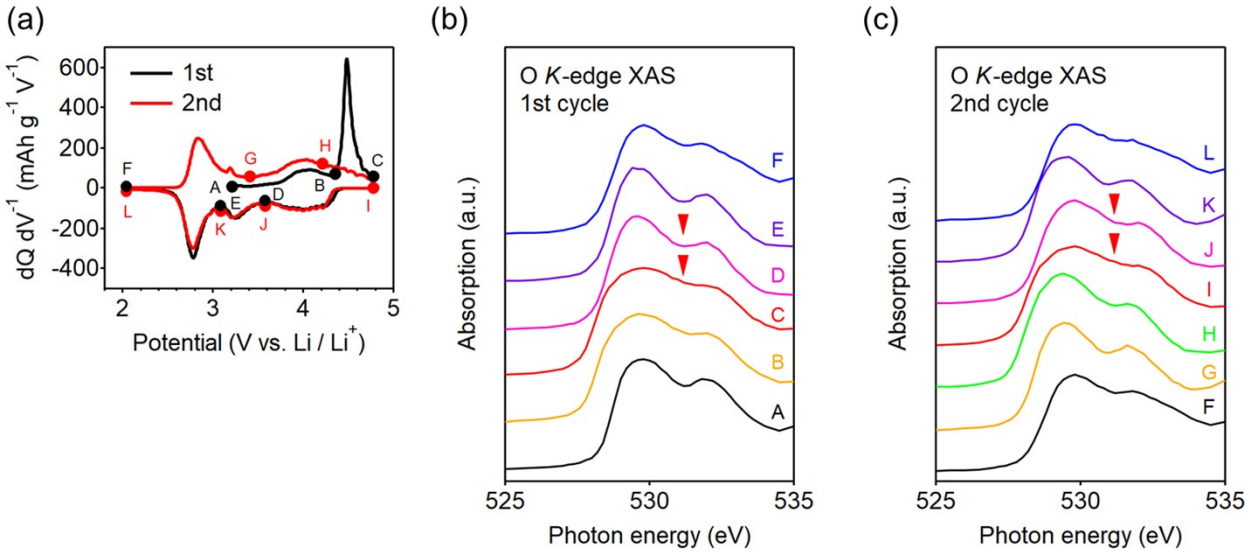

Figure S6. (a) The dQ/dV plots of O2-$Li_{1.12-y}Ni_{0.17}Mn_{0.71}O_2$ during the first and second cycle at the charge/discharge rate of C/20, and *ex situ* O *K*-edge X-ray absorption spectra (XAS) during (b) the first and (c) second charge/discharge cycles. Red triangles indicate the absorption for oxidized oxygen.

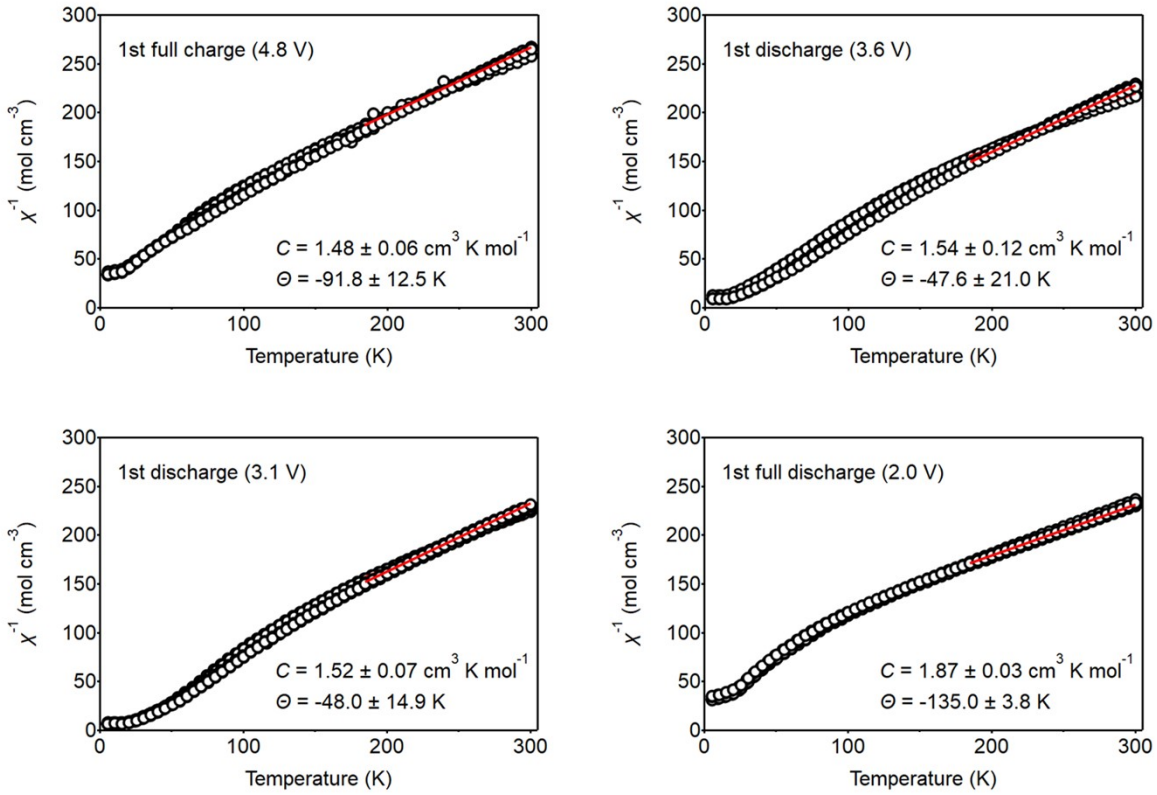

Figure S7. Inverse of the magnetic susceptibility (χ) as a function of temperature for O2-$Li_{1.12-y}Ni_{0.17}Mn_{0.71}O_2$ during the first discharge process. The Curie constant (C) and Weiss temperature (Θ) at each state-of-discharge are average values for three samples.

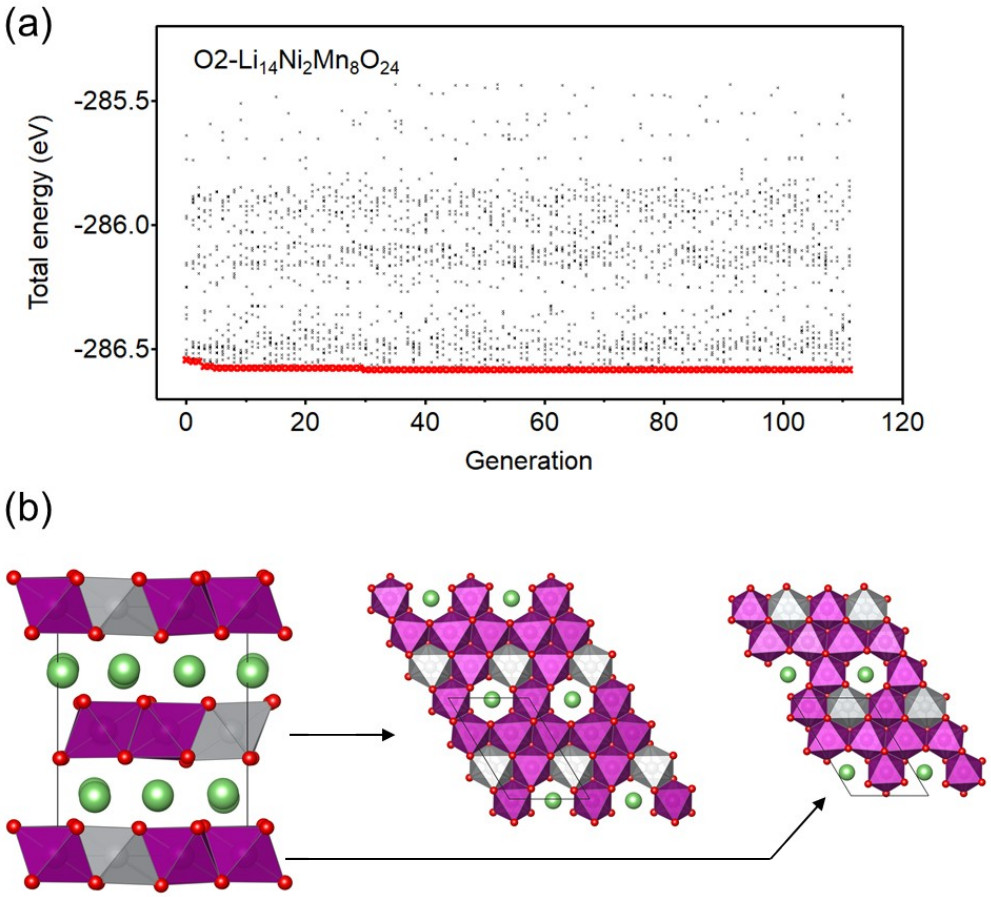

Figure S8. Variation of total electron energies for genetic algorithm (GA) driven structures as a function of generation. The red symbols indicate the lowest energy of GA generated structures among present and previous generations. (b) The optimized Li/Ni/Mn arrangement for O2-type $Li_{14}Ni_2Mn_8O_{24}$ (≈ $Li_{1.17}Ni_{0.17}Mn_{0.67}O_2$). Purple and silver colored octahedra and green spheres correspond to MnO_6, NiO_6, and Li atom, respectively.

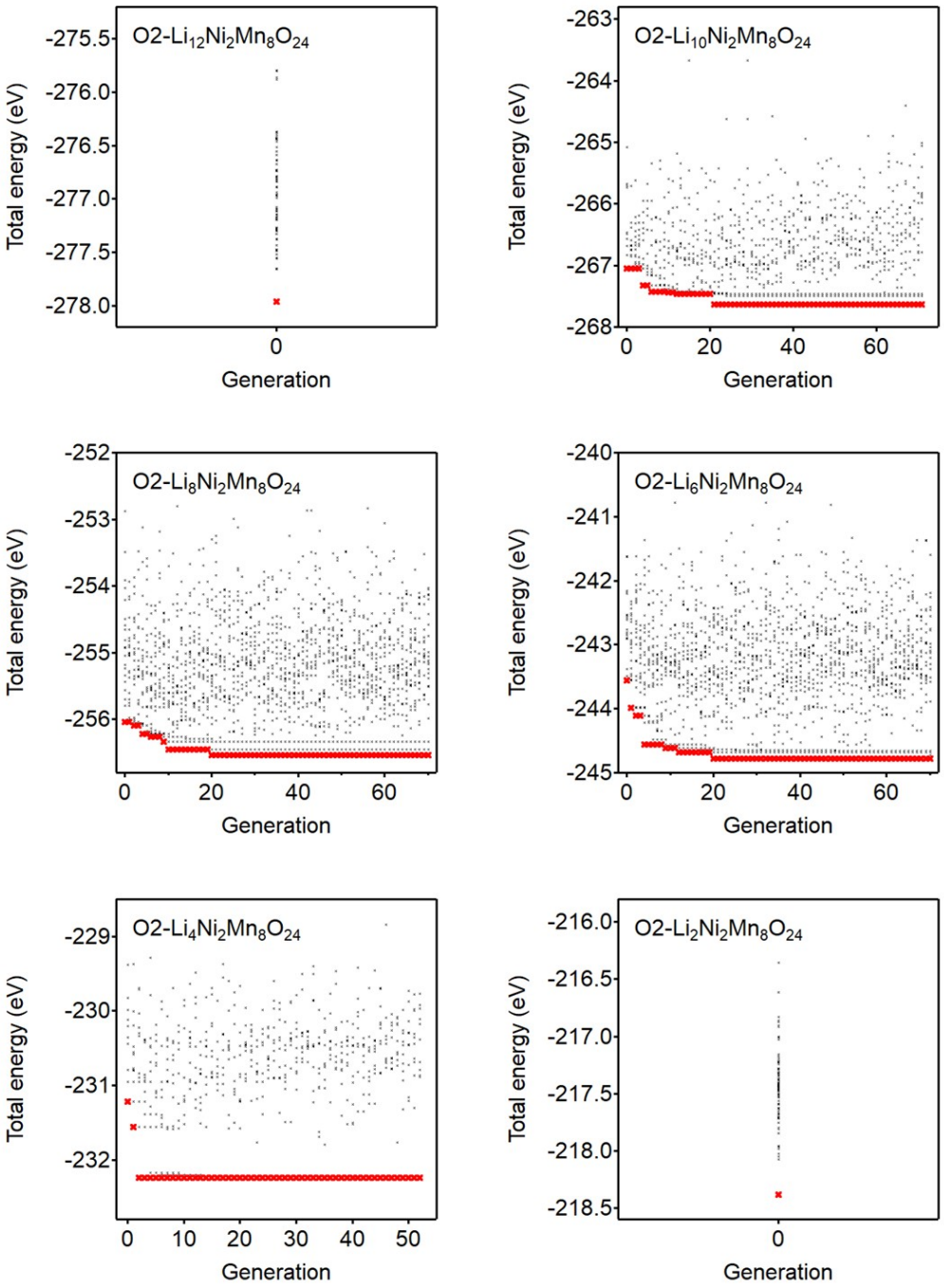

Figure S9. Variation of total electron energies for genetic algorithm (GA) driven structures as a function of generation for each Li composition z in $Li_{14-z}Ni_2Mn_8O_{24}$. The red symbols indicate the lowest energy of GA generated structures among present and previous generations.

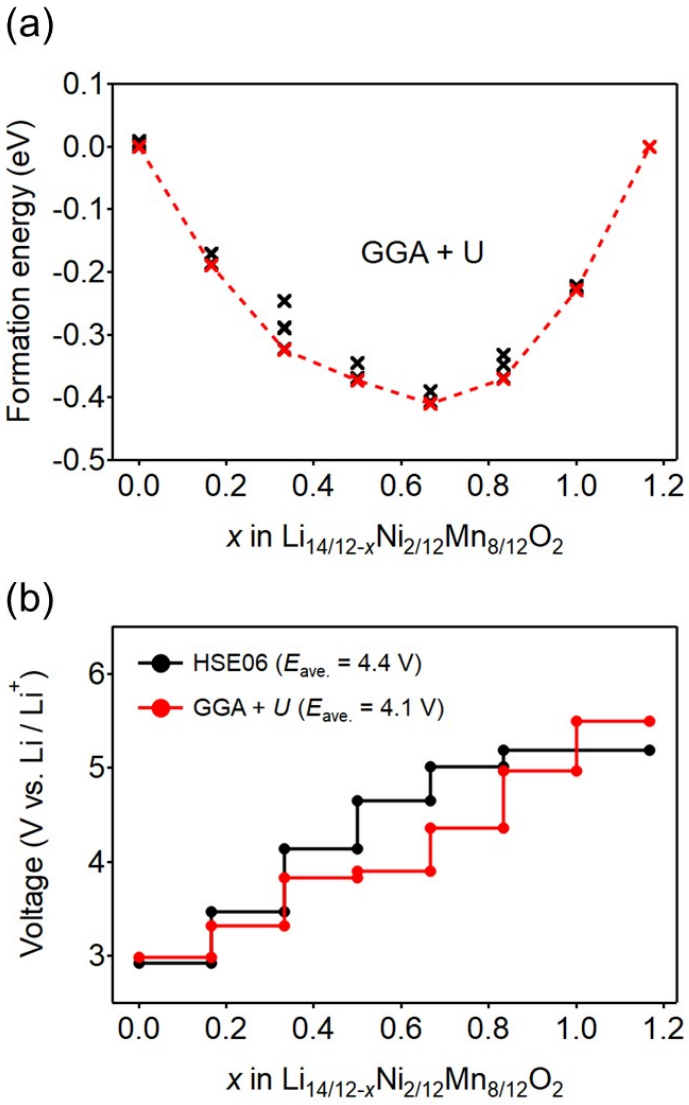

Figure S10. (a) Formation energies of genetic algorithm (GA) driven structures. Red crosses connected with dashed line and black crosses indicate the convex hull and energies of the 2nd–5th stable structures with different Li/Ni/Mn arrangements. (b) Calculated voltages as a function of Li composition x in $Li_{14/12-x}Ni_{2/12}Mn_{8/12}O_2$. The inset shows the overall view of the calculated voltages.

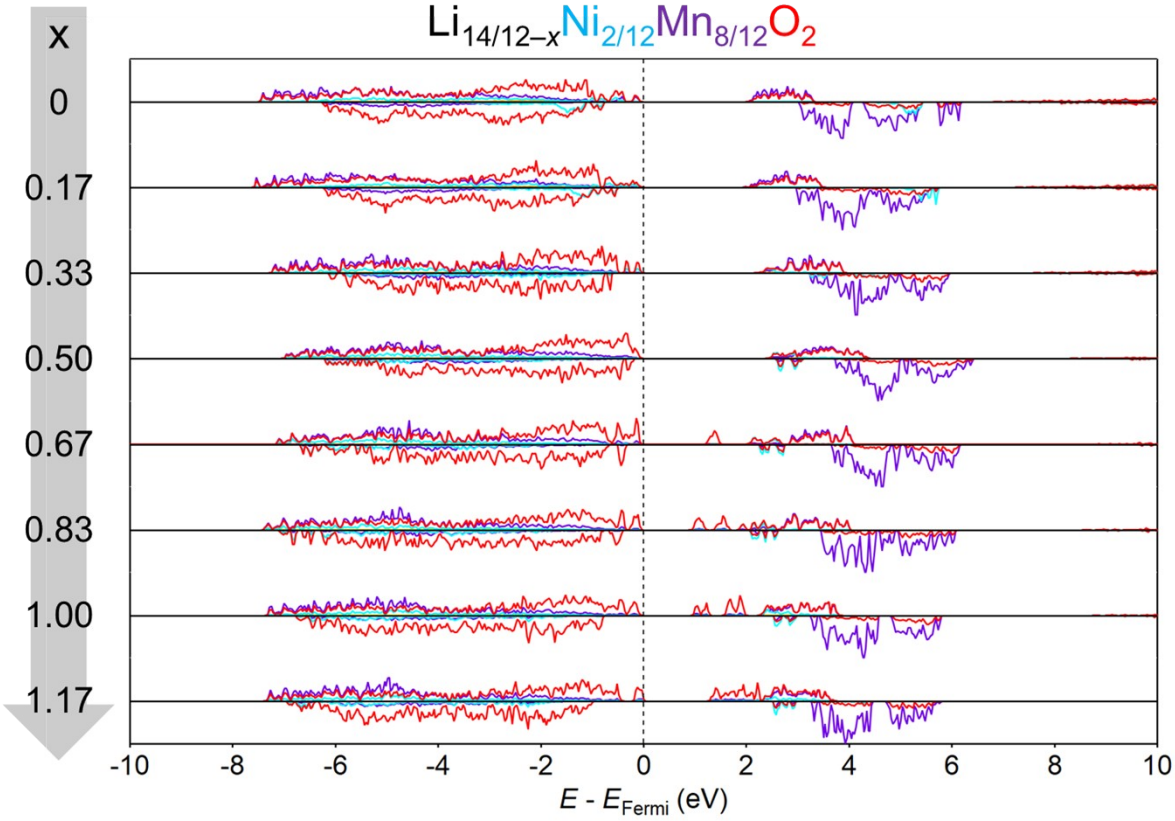

Figure S11. Projected density of states (pDOS) calculated by HSE06 functional as a function of Li composition x in $Li_{14/12-x}Ni_{2/12}Mn_{8/12}O_2$. Sky blue, purple, and red lines indicate pDOS of Ni, Mn, and O, respectively.

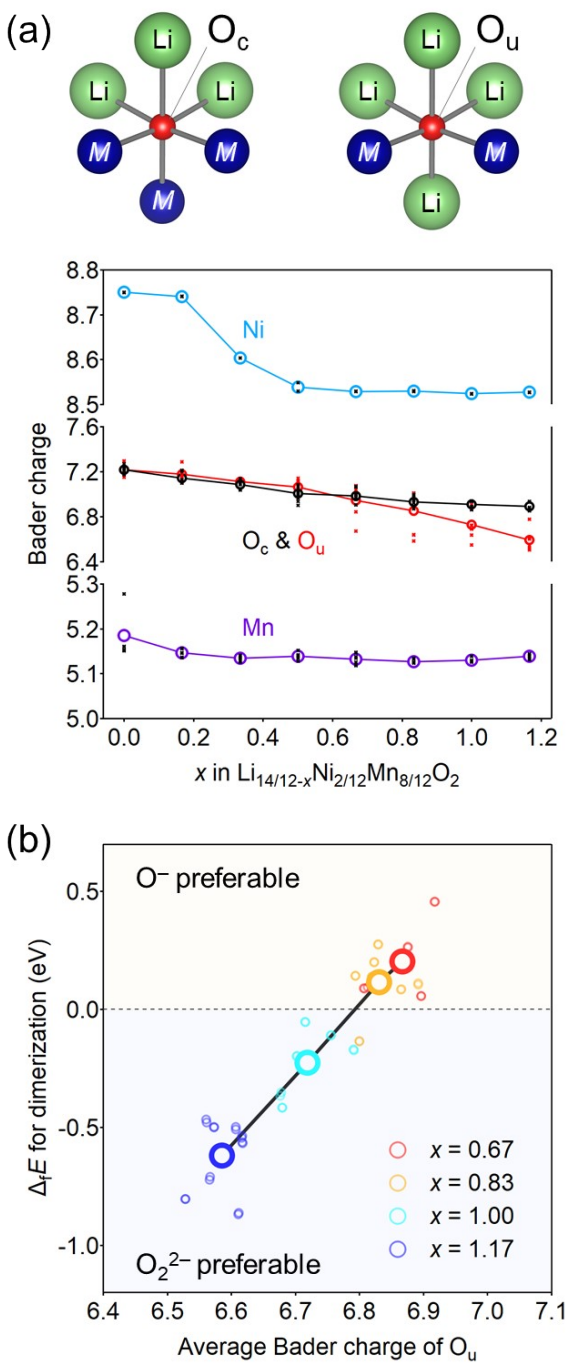

Figure S12. (a) The variation of Bader charge as a function of Li composition x in $Li_{14/12-x}Ni_{2/12}Mn_{8/12}O_2$. Colored circles are averaged values. Oxygen coordinated by three transition metals is denoted as O_c, while oxygen coordinated by two transition metals is denoted as O_u. (b) Formation energy of O_u–O_u dimers ($\Delta_f E$) as a function of as a function of average Bade charge of dimerizing O_u. Each bold circle corresponds to an averaged point for each x. No O_c–O_u dimerization occurs.

Rate constant for dimerization of O^- under a CCCV (float) mode

Let us consider the dimerization of two O^- with a rate constant k [$cm^3\ mol^{-1}\ s^{-1}$],

$$2O^- \rightarrow O_2^{2-}$$

When an oxygen oxidation process at a specific current of j [mA/g] starts from $t = 0$ [s], the concentration of O^-, C_r [mol/cm^3], changes as,

$$\frac{dC_r}{dt} = -kC_r^2 + \frac{j\rho}{F}$$

where ρ [g/cm^3] is the density of an electrode material. Let $\alpha = \sqrt{\frac{j\rho}{F}}$, then this differential equation can be solved for $C_r < \alpha k^{-\frac{1}{2}}$ as,

$$C_r(t) = \frac{\alpha k^{-\frac{1}{2}}\left\{1 - \exp\left(-2\alpha k^{\frac{1}{2}} t\right)\right\}}{1 + \exp\left(-2\alpha k^{\frac{1}{2}} t\right)}$$

Note that $C_r(t = 0) = 0$, and $C_r < \alpha k^{-\frac{1}{2}}$ is satisfied for $0 < t < +\infty$.

During a constant-voltage mode ($t_1 < t < t_2$), C_r changes as a function of time t as,

$$\frac{dC_r}{dt} = -kC_r^2$$

which leads to,

$$C_r(t) = \frac{1}{\frac{1}{C_r(t = t_1)} + k(t - t_1)}$$

Note that we assume no parasitic side reactions when applying the constant voltage.

When a discharge at a specific current of j starts from $t = t_2$, C_r changes as,

$$\frac{dC_{\mathrm{r}}}{dt} = -kC_{\mathrm{r}}^{2} - \frac{j\rho}{F}$$

This differential equation can be solved as,

$$C_{\mathrm{r}}(t) = \alpha k^{-\frac{1}{2}} \tan\left(\alpha k^{\frac{1}{2}}\left(t_2 - t\right) + \arctan\frac{C_{\mathrm{r}}(t_2)}{\alpha k^{-\frac{1}{2}}}\right)$$

Therefore, $C_{\mathrm{r}}(t)$ is summarized as,

Charge (oxygen oxidation)

$$C_{\mathrm{r}}(t) = \frac{\alpha k^{-\frac{1}{2}}\left\{1 - \exp\left(-2\alpha k^{\frac{1}{2}} t\right)\right\}}{1 + \exp\left(-2\alpha k^{\frac{1}{2}} t\right)} \text{ for } 0 < t < t_1$$

Constant voltage

$$C_{\mathrm{r}}(t) = \frac{1}{\frac{1}{C_{\mathrm{r}}\left(t = t_1\right)} + k\left(t - t_1\right)} \text{ for } t_1 < t < t_2$$

Discharge

$$C_{\mathrm{r}}(t) = \alpha k^{-\frac{1}{2}} \tan\left(\alpha k^{\frac{1}{2}}\left(t_2 - t\right) + \arctan\frac{C_{\mathrm{r}}(t_2)}{\alpha k^{-\frac{1}{2}}}\right) \text{ for } t_2 < t$$

For example, Figure S13 shows $C_{\mathrm{r}}(t)$ under the CCCV condition of (1) charge at 20 mA/g for 3 h, (2) constant-voltage application for 3h, and then (3) discharge at 20 mA/g. Here, $k = 0.01$ [$\mathrm{cm^3\ mol^{-1}\ s^{-1}}$] and $\rho = 5.0$ [$\mathrm{g/cm^3}$].

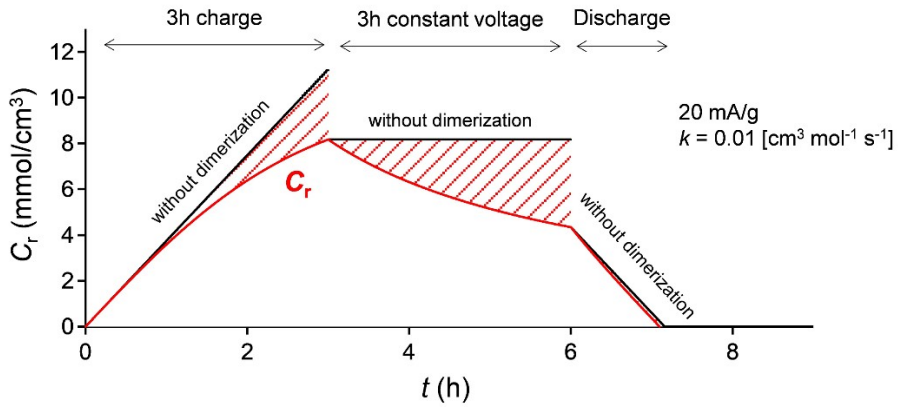

Figure S13. $C_r(t)$ under the CCCV condition of charge at 20 mA/g for 3 h, constant-voltage application for 3h, and then discharge at 20 mA/g. Black line: no dimerization reaction, read line: dimerization at the rate constant of $k = 0.01$ [cm³ mol⁻¹ s⁻¹].

As the formation of O_2^{2-} during discharge is negligible (Figure S13), the discharge capacity Q [mAh/g] for $O_2^{2-} \rightarrow O_2^{4-}$ as a function of the constant-voltage duration $\Delta t = t_2 - t_1$ is calculated as,

$$Q(\Delta t) = \frac{F}{\rho}\left\{\alpha^2 t_1 - \frac{1}{\frac{1}{C_r(t_1)} + k\Delta t}\right\}$$

Figure S14 shows the dQ/dV plots for discharging O2-$Li_{1.12-y}Mn_{0.71}Ni_{0.17}O_2$ after different constant-voltage durations (from 0 h to 48 h).

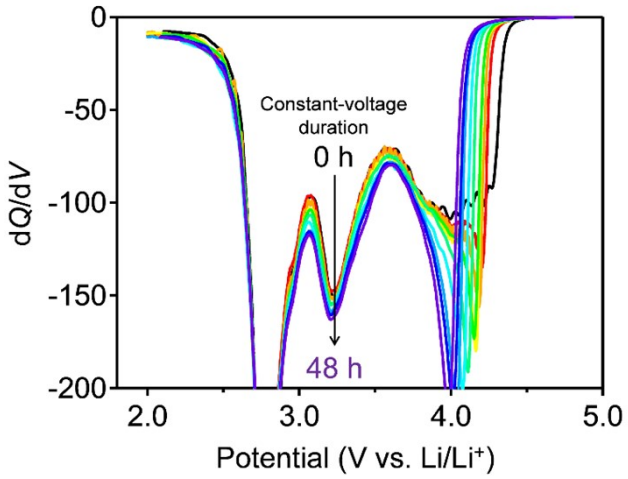

Figure S14. The dQ/dV plots for discharging O2-$Li_{1.12-y}Mn_{0.71}Ni_{0.17}O_2$ after different constant-voltage

durations (from 0 h to 48 h).

Based on these plots, it is possible to derive $Q(\Delta t)$(for example, using Gaussian fitting). Figure S15 is the plot of $Q(\Delta t)$ (blue empty circles) with a fitted result (black dotted line), providing the dimerization-rate constant $k = 3.5 \times 10^{-2}$ [cm^3 mol^{-1} s^{-1}].

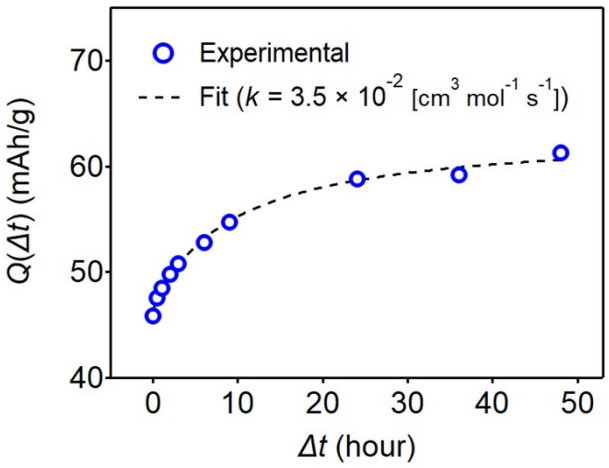

Figure S15. Discharge capacity Q [mAh/g] for $O_2^{2-} \rightarrow O_2^{4-}$ as a function of the constant-voltage duration $\Delta t = t_2 - t_1$. Blue empty circles are experimental, and a black dotted line is a fitted result.

Using the obtained k, the concentrations of O^- (red solid line) and O_2^{2-} (blue solid line) in O2-$Li_{1.12-y}Mn_{0.71}Ni_{0.17}O_2$ can be simulated as a function of time (Figure S16 for the condition of no constant-voltage application, and Figure S17 for the condition of 3 h constant-voltage application). Here, $j = 16.9$ [mAh g^{-1}] and $\rho = 4.28$ [g/cm^3], and the oxidation reactions of $O^{2-/-}$ and $Ni^{4+/3+/2+}$ were assumed to occur simultaneously at the late stage of charge.

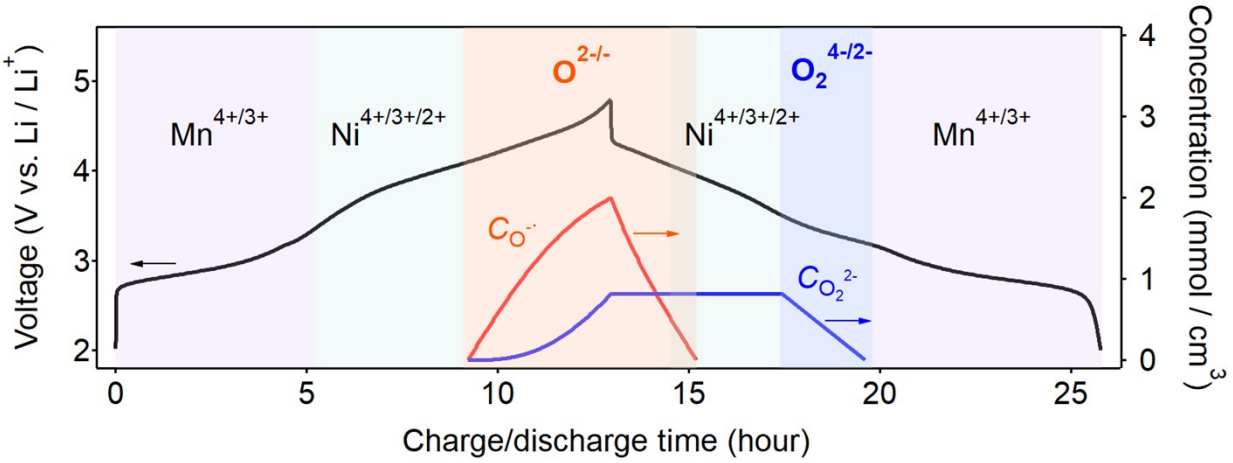

Figure S16. Time dependence of the concentrations of O^- (red solid line) and O_2^{2-} (blue solid line) in O2-$Li_{1.12-y}Mn_{0.71}Ni_{0.17}O_2$ under the condition of no constant-voltage application.

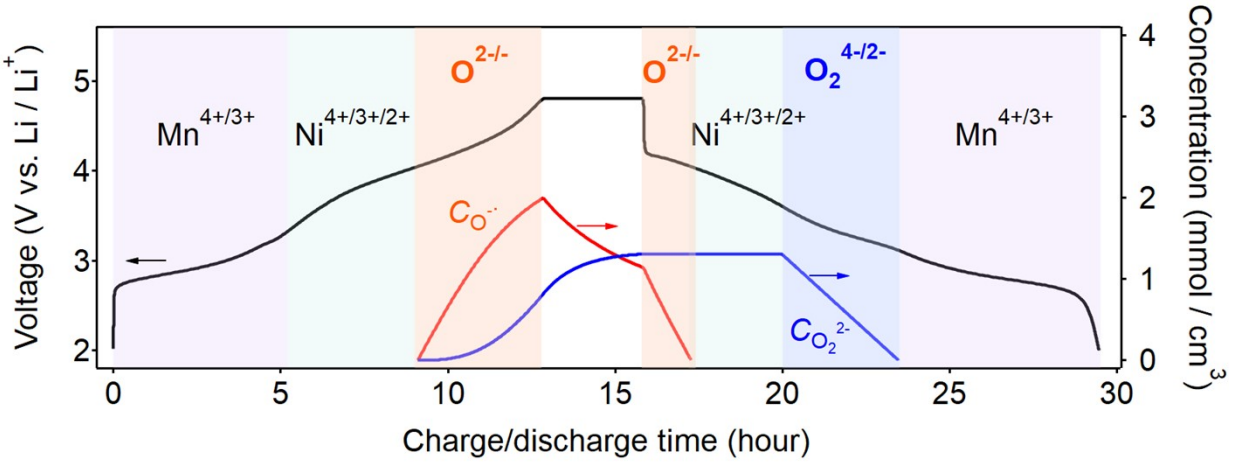

Figure S17. Time dependence of the concentrations of O^- (red solid line) and O_2^{2-} (blue solid line) in O2-$Li_{1.12-y}Mn_{0.71}Ni_{0.17}O_2$ under the condition of 3 h constant-voltage application.

As shown in Figures S16 and S17, O^- dimerizes to O_2^{2-} during charge and constant-voltage processes, providing the discharge capacity for $O_2^{2-} \rightarrow O_2^{4-}$ at 3.3 V vs. Li/Li$^+$. With increasing the duration of constant-voltage application, the concentration of O_2^{2-} increases to give larger discharge capacity for $O_2^{2-} \rightarrow O_2^{4-}$, as observed in Figure S15. Therefore, the oxygen redox reaction in Li-rich layered oxides can be summarized as a square scheme shown in Figure S18.

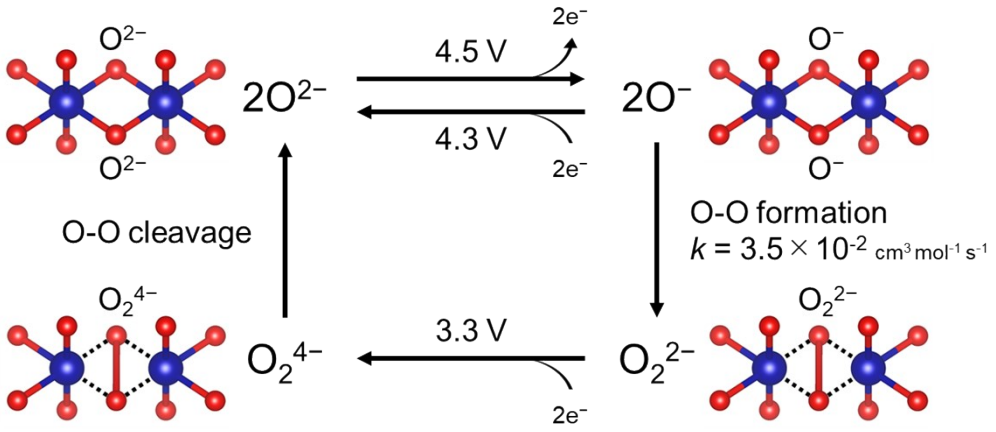

Figure S18. Square scheme for oxygen-redox reaction in Li-rich layered oxides.

Finally, assumptions in this calculation are listed below.

(1) j is much smaller than Li$^+$ diffusivity (homogeneous reaction, no Li$^+$ concentration gradient)

(2) $O^- + O^{2-} \rightarrow O_2^{2-} + e^-$ does not occur.

(3) The electrode potential (E) of O2-$Li_{1.12-y}Ni_{0.17}Mn_{0.71}O_2$ is dominated mainly by μ_{Li} at a deep state-of-charge.

(4) The oxidation reactions of $O^{2-/-}$ and $Ni^{4+/3+/2+}$ occur simultaneously at the late stage of charge.

(5) No heterogeneous reaction occurs within the composite electrode (single-particle approximation)

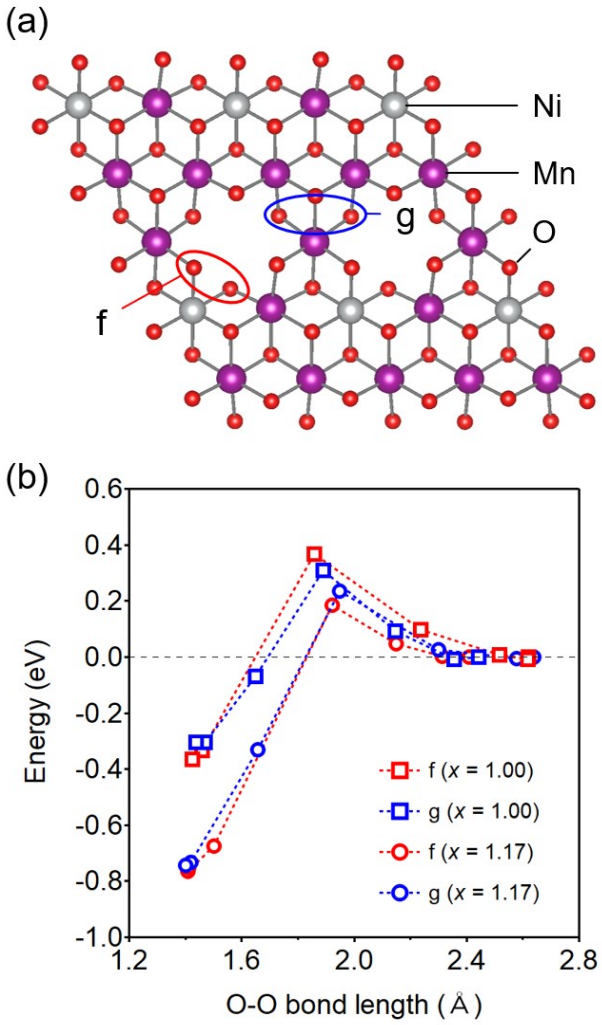

Figure S19. Calculated energy barrier for O-O dimerization in delithiated structures. (a) atomic positions of dimers, (b) Energy diagram as a function of the O-O bond length obtained by a nudged elastic band method.

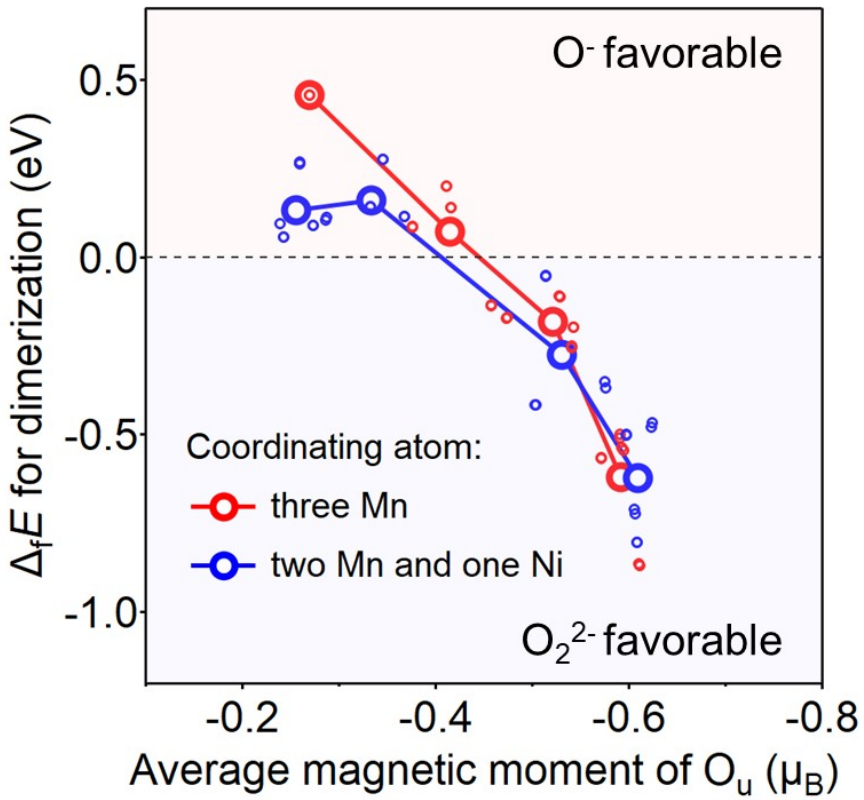

Figure S20. Formation energy of O_u–O_u dimers ($\Delta_f E$) as a function of an average magnetic moment of dimerizing O_u atoms. Each bold circle corresponds to an averaged point for each x in $Li_{14/12-x}Ni_{2/12}Mn_{8/12}O_2$. $\Delta_f E$ for O_u–O_u pairs coordinated to Ni is lower than that to Mn.